International Journal of Mechanical Sciences 254 (2023) 108407

Contents lists available at ScienceDirect

International Journal of Mechanical Sciences

journal homepage: www.elsevier.com/locate/ijmecsci

Sommerfeld effect in a vibrocompaction process

Javier González-Carbajal *, Daniel García-Vallejo, Jaime Domínguez

Department of Mechanical Engineering and Manufacturing, University of Seville, Spain

ARTICLE INFO

Keywords:
Vibrocompaction
Sommerfeld effect
Nonideal excitation
Granular materials

ABSTRACT

This study addresses the influence of the Sommerfeld effect on the behaviour of vibrocompacting machines driven by unbalanced electric motors. Based on a simplified model with 4 degrees of freedom previously published by the authors, we investigate the dynamics of quasistatic vibrocompaction processes, i.e. those in which the compaction is achieved through a sufficiently slow increase in the input power of the electric motors. The main novel contribution of the paper is the characterization of the evolution of the system state through a *quasistatic torque curve*, which is analytically derived. This curve provides the maximum compaction that can be quasistatically achieved and the amount of motor torque required to reach a desired compaction level, while also revealing the specific way in which the Sommerfeld effect takes place in the system under study. The analytical results are used to give a clear physical interpretation to the numerical results previously published by the authors. Good agreement is found between numerical and analytical results.

1. Introduction

The need to compact granular materials is often encountered in different engineering fields, such as geotechnics [1], aerospace engineering [2] and manufacturing [3–5]. Vibrating machines constitute an efficient and widely used means to meet this objective, by producing a denser packing of the material grains [6,7]. We also note that the propagation of nonlinear elastic waves in granular materials has received considerable scientific attention in the last years [8–10]. Specifically, this work has been motivated by the authors' interest in the manufacturing of quartz agglomerates, one of whose most crucial stages is the vibrocompaction of a quartz-resin mixture by using unbalanced electric motors, together with a vacuum system [11,12].

The present paper can be seen as an extension of a previous work published by the authors, where a nonlinear model for the vibrocompaction of quartz agglomerates was presented and justified [13]. This model was numerically investigated in [13] by conducting representative simulations that allowed assessing the effect of different machine parameters on the final result of the compaction process. It is worth noting that relevant nonlinear behaviour was observed in these simulation results resembling the typical features of the well-known Sommerfeld effect, which occurs due to reciprocal interaction between a vibrating system and its energy source [14]. However, the physical interpretation of these phenomena was not straightforward due to the increased complexity of the model with respect to those generally used to investigate the Sommerfeld effect. This article intends to provide significant insight into the vibrocompaction dynamics through a detailed analytical investigation of the model.

It is worth stressing the high interest of this type of research from an industry perspective. The ability to better understand and predict the behaviour of vibrocompacting machines would allow to optimize their design and to properly tune their parameters for each specific scenario. On the other hand, the originality of this work is attested by the fact that no previous investigation on the Sommerfeld effect in vibrocompaction systems is available in the literature, to the best of the authors' knowledge.

This introduction is divided into two subsections. In the first one, a description of the industrial vibrocompaction process of interest is presented. The second subsection provides a summary and literature review on the Sommerfeld effect.

1.1. The vibrocompaction of quartz agglomerates

Quartz agglomerates are very frequently used as an artificial stone for countertops in kitchens and bathrooms [15,16]. The production of a slab of this material includes the mixing of the quartz grains with a polyester resin, the vacuum vibrocompaction of the mixture, the polimerization of the resin in a kiln and the machining of the slab after cooling [17]. It should be stressed that the compaction step is crucial for the result of the manufacturing process, since it avoids the presence of pores on the surface of the final countertop. These pores tend to accumulate dirt and are particularly difficult to clean. In fact, the detection of a pore of sufficient size during the quality control of the process implies the rejection of the slab.

* Corresponding author.
E-mail addresses: jgcarbajal@us.es (J. González-Carbajal), dgvallejo@us.es (D. García-Vallejo), jaime@us.es (J. Domínguez).

https://doi.org/10.1016/j.ijmecsci.2023.108407
Received 23 November 2022; Received in revised form 12 April 2023; Accepted 23 April 2023
Available online 2 May 2023

In order to better understand the nature of the compaction, note that the mixture is initially composed of three different phases: solid (the quartz grains), liquid (the resin) and gas (air). The air is present in two ways: as bubbles within the resin and as gaps among the quartz grains that the resin has not been able to fill. The aim of the compaction is to evacuate this air, considerably reducing the thickness of the slab.

The vibrocompaction process takes place as follows. First, a heavy piston on which the unbalanced motors are mounted descends onto the mould containing the material to be compacted. The piston, which has the dimensions of the slab, exerts initially a static pressure on the mixture due to its own weight and to an external air pressure applied on it. Then, the air pressure inside the mould is reduced by means of a vacuum system. Finally, the electric motors are switched on, producing the vibration needed to complete the compaction. During this dynamic process, separations and impacts can occur between the piston and the mixture, and also between the mixture and the mould [18].

It is easy to note the high complexity of the physics involved in this process, with the final result of the compaction depending on a large number of factors: granulometry of the quartz, rheological properties of the resin, amount of unbalance, available power of the electric motors, weight of the piston, etc [19,20]. Notice also that there are several sources of nonlinearity in the vibrocompacting system, the most relevant of them being:

- The constitutive behaviour of the mixture. The mechanics of granular materials is a very complex subject that has received wide attention in the scientific literature [21–24]. Clearly, any model that intends to represent the mechanical response of a quartz-resin mixture being compacted needs to be nonlinear, in order to account for irreversible deformation. In fact, a material model based on first principles would need to include the motion of the bubbles through the mixture, the friction between quartz particles, the interaction between quartz and resin, etc [25]. Thorough investigations on the behaviour of three-phase mixtures, granular media and porous materials can be found elsewhere [26–30]. As a powerful alternative to models based on first principles, it is often useful to resort to phenomenological models that can capture the global behaviour of the material, as has been done in [13].
- The possibility of having separations and impacts at the mixture-piston and mixture-mould contacts.
- The dynamic interaction itself between the machine vibration and the rotation of the motors. This particular nonlinearity is usually referred to as *the Sommerfeld effect*, and is briefly described in the next subsection.

1.2. The Sommerfeld effect

In the analysis of forced vibrations, it is customary to implicitly assume that the external excitation is a known function of time. This is generally known as the assumption of *ideal excitation*. However, since the experimental work of Sommerfeld in 1904 [31], it is known that some kinds of behaviour found in mechanical systems cannot be explained upon the ideality hypothesis. In other words, there are situations in which the excitation has to be considered as *nonideal*, meaning that it is influenced by the motion of the system [32].

Sommerfeld's findings were based on a setup consisting in an unbalanced electric motor mounted on an elastic support. During the tests, the motor input power was gradually increased/decreased, making the rotor speed pass through the system's resonance frequency in both directions [33]. The results of a numerical simulation of Sommerfeld's test are displayed in Fig. 1. The points on the graph represent the obtained stationary states when the motor input power is varied linearly with time in small equal steps (after each step, the motor control is kept constant until a stable motion is attained). The figure shows the interesting phenomenon that certain range of rotor speeds cannot be reached. The reason is that, at some point in the process, the system experiences a sudden jump, both in rotor speed and oscillation amplitude (note that the jump is different for increasing and decreasing input power). This is the essence of what is usually called *the Sommerfeld effect*.

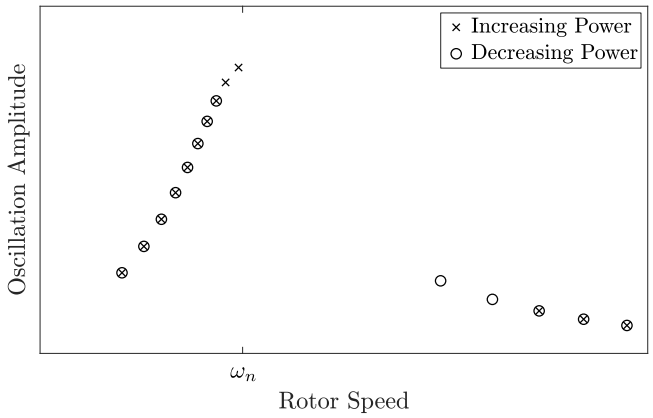

Fig. 1. Numerical simulation of Sommerfeld's experiment. The motor input power is varied linearly with time in small equal steps. After each step, the motor control is kept constant until the system reaches a stationary state. These points of stable motion are represented on the graph. The natural frequency of the vibrating system is denoted as ω_n.

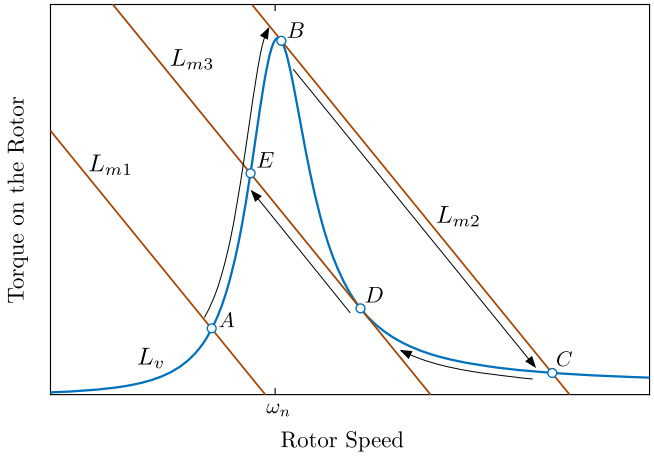

Fig. 2. Graphical explanation for the Sommerfeld Effect according to Kononenko [34]. Curves L_{mi} $(i = 1, 2, 3)$ represent the motor characteristics at different time instants, while L_v corresponds to the torque on the rotor due to vibration. Jump phenomena occur from point B to C for increasing input power and from point D to E for decreasing input power.

Years later, Kononenko used averaging techniques to obtain the stationary motions of Sommerfeld's system as the intersections between two functions: the torque–speed curve of the motor, L_m, and a curve representing the torque on the rotor due to vibration, L_v (see Fig. 2) [34]. Assuming that the motor is controlled by displacing its torque–speed curve parallel to itself, Fig. 2 shows how Kononenko's representation accounts for Sommerfeld's experimental results: the state of the system experiences a jump phenomenon when tangency point B or D is reached for increasing or decreasing input power, respectively [34–37].

It is interesting to note that the previous description assumes that all solutions between points A and B, and between C and D, are stable. However, it was proved in [38,39] that some of the solutions between C and D can actually be unstable under certain conditions. This means that the jump phenomenon for decreasing input power can occur before predicted in Fig. 2.

After the works of Sommerfeld and Kononenko, substantial research effort has been devoted to the study of vibrating systems excited by nonideal power sources, and the particular dynamics that they can exhibit. Sghaier et al. addressed the coupling of bending and torsional vibrations of rotors under nonideal excitation [40]. Varanis et al. [41] used the continuous wavelet transform to study the Sommerfeld effect on an oscillator with fractional damping. Avanço et al. applied bifurcation analysis to control the appearance of chaotic behaviour on a nonideally driven electromechanical pendulum [42]. Palacios Félix et al. demonstrated that nonideal systems can be used for energy harvesting purposes [43]. The mitigation of nonideally excited oscillations by linear vibration absorbers was addressed by Piccirillo [44]. Drozdetskaya et al. investigated the case of an elastically supported electric motor with two coaxial unbalances [45]. Bharti et al. coined the term *Sommerfeld effect of second kind* [46], referring to a variant of the classical Sommerfeld effect associated with the instability of the rotor whirl, and presented a numerical study of the phenomenon. A methodology to mitigate the Sommerfeld effect by properly tuning the external damping of the system was described by Jha and Dasgupta [47]. Kong et al. analysed the particular problem of a simply supported beam excited by two nonideal unbalanced motors [48]. They also focused on the self-synchronization between both motors during the beam oscillation. The wavelet synchrosqueezed transform was used by Varanis et al. to investigate the dynamics of nonideally excited systems [49]. Bharti et al. performed a numerical investigation on the appearance of the Sommerfeld effect in the torsional vibrations of a double-Cardan joint driveline [50].

Although most analytical works on nonideally excited oscillations used averaging techniques to simplify the equations of motion [33,35,38,51], the method of *direct separation of motions*, first introduced by Blekhman [52], has also proved to be a powerful analytical tool for the study of nonideal systems [53,54].

In terms of experimental works, it is worth mentioning some recent investigations by Varanis et al. where different setups—a cantilever beam, a portal frame, a shear-building structure—are used for experimental validation of theoretical results [55,56]. Also relevant are the investigation of the nonideal behaviour of electrodynamic shakers in [57] and the experimental demonstration offered by Kossoski et al. on the mitigation of the Sommerfeld effect by means of shape memory alloys [58]. For a more detailed literature review, the interested reader is referred to [59,60].

As is clear from the above lines, the Sommerfeld effect is a relevant nonlinear phenomenon that can significantly affect the behaviour of such varied engineering systems as beams, pendulums, energy harvesting devices, rotors, Cardan joints, portal frames or shape memory alloys. However, to the best of the authors' knowledge, there are no previous works in the literature addressing the impact of the Sommerfeld effect on vibrocompacting machines.

In this work, the dynamics of vibrocompacting machines driven by unbalanced electric motors will be analysed using a simplified analytical model. This will provide a good understanding of the appearance of the Sommerfeld effect in the system and a useful physical interpretation to the numerical results previously published by the authors [13].

The paper is structured as follows. Section 2 presents a simplified mathematical model for vibrocompaction that can be treated analytically. Section 3 makes use of this model to study the appearance of the Sommerfeld effect in quasistatic vibrocompaction processes. In Section 4, the obtained analytical results are used to provide a clear physical interpretation to the numerical results previously published by the authors. The good agreement between analytical and numerical results also serves as a validation of the presented analytical developments. Finally, Section 5 puts forth the main conclusions of the study.

2. Simplified model and torque–speed curves

The present investigation is based on a 4-degree-of-freedom (4-DOF) vibrocompaction model previously published by the authors [13], which is briefly described in Appendix A. Our analysis also builds upon some classical results on the response of linear systems to the nonideal excitation provided by unbalanced motors, which are summarized in Appendix B.

Regarding the reasons for choosing a 4-DOF model, some comments are pertinent. It is clear that modelling the dynamics of a vibrocompaction machine driven by an unbalanced motor requires at least 2 DOFs: one for the rotation of the motor and one for the displacement of the piston on which the motor is mounted. However, if the model is intended to consider separations and impacts at the top and at the bottom of the mixture being compacted, two additional DOFs are needed (one for each of the contacts). Hence, 4 is the minimum number of DOFs that allows modelling the system of interest allowing for separations. Of course, more complex and realistic models could be built with additional DOFs. For example, more DOFs could be included to model several vibration modes of the mixture. The philosophy behind this work is to start the analysis of the vibrocompacting system with a low-dimension tractable model that facilitates the interpretation of results. Future steps in this line of research will include considering additional DOFs for more accurate predictions.

Even though the 4-DOF vibrocompaction model is, of course, very simplified with respect to real vibrocompacting machines, it is still too complex for an analytical treatment of the equations of motion. Section 2.1 shows that, under reasonable assumptions, the 4-DOF model can be reduced to a more tractable 2-DOF model. Furthermore, it is shown that the results presented in Appendix B can be applied to the 2-DOF vibrocompaction model. Particularly useful is the possibility to obtain the stationary motions of the machine as the intersections between the motor torque curve and the vibration torque curve, as described in Appendix B. Section 2.2 addresses the main particularity of the vibration torque curves for the vibrocompaction system: since the mixture stiffness is not fixed, but increases as the compaction progresses, the system will exhibit a family of infinite curves, one for each possible value of the mixture stiffness.

2.1. Simplified model

In order to simplify the model summarized in Appendix A, consider the following assumptions:

- The motion of interest occurs without separations between mixture and piston nor between mixture and mould. This implies $y_t = y_p$, $y_b = 0$ in Eq. (A.1), which means that the number of DOFs is reduced to 2 (y_p, y_t and y_b represent the vertical positions of the piston, the top surface of the mixture and the bottom surface of the mixture, respectively).
- Since the simplified model will be used to investigate the stationary motions of the machine, it is reasonable to assume also that the nonlinear spring representing the mixture (see Fig. A.1) is only subjected to elastic deformation. The reason is that, once the system has reached a stationary state of motion, there is no further compaction and the spring force, F_m, follows a straight line in the force–displacement graph, such as segment AB in Fig. A.2, with certain stiffness $k_i \in [k_0, k_f]$. Parameters k_0 and k_f represent the stiffness of the uncompacted and fully compacted mixture, respectively (see Appendix A for more details).

With these two assumptions, system (A.1) can be written as

$$\begin{aligned} m\ddot{x} + b\dot{x} + k_i x &= m_1 r(\dot{\phi}^2 \cos\phi + \ddot{\phi}\sin\phi) \\ I\ddot{\phi} &= L_m(\dot{\phi}) + m_1 r \sin\phi(\ddot{x} + g) \end{aligned} \tag{1}$$

where $m = m_p + m_m/3 + m_1$ and $I = I_0 + m_1 r^2$. Parameter m_p stands for the mass of the piston and the motor, m_m is the mass of the mixture, m_1

is the unbalanced mass, I_0 is the rotor inertia, r is the eccentricity of the unbalance, b is the damping coefficient, g is the gravity constant, x represents the displacement of the piston with respect to its static equilibrium position, ϕ represents the angular position of the rotor and an overdot represents differentiation with respect to time.

$L_m(\dot{\phi})$ is the driving torque provided by the motor, which is assumed to be a linear function of the rotor speed:

$$L_m(\dot{\phi}) = C + D\dot{\phi}, \tag{2}$$

We note that the derivation of system (1) simply requires performing the substitutions $y_t = y_p$, $y_b = 0$, $\dot{y}_p = \dot{x}$, $\ddot{y}_p = \ddot{x}$ and $F_m + mg = k_i x$ on system (A.1). Then, adding up the first two equations in system (A.1) provides the first equation in system (1), while the fourth equation in system (A.1) becomes the second equation in system (1).

The gravity term in Eq. (1) can be shown to have no significant effect for the purposes of this investigation. The reason is that the stationary motions of the system will be obtained using the method of direct separation of motions, proposed by Blekhman [52]. This approach, which has some similarities with classical averaging techniques [61], includes the averaging of the equations of motion in order to find the mean values of rotor speed and vibrating amplitude. Since the gravity term, $m_1 r g \sin\phi$, becomes zero when averaged over angle ϕ, it does not affect the mean stationary rotor speed or oscillation amplitude (see [52,62] for details). Hence, Eq. (1) can be rewritten as

$$\begin{aligned} m\ddot{x} + b\dot{x} + k_i x &= m_1 r(\dot{\phi}^2 \cos\phi + \ddot{\phi}\sin\phi) \\ I\ddot{\phi} &= L_m(\dot{\phi}) + m_1 r\ddot{x}\sin\phi \end{aligned} \tag{3}$$

Note that system (3) is exactly the same as system (B.1), which allows applying the general results presented in Appendix B to the vibrocompaction model. In the remainder of the paper, we will refer to systems (A.1) and (3) as the *full model* and the *simplified model*, respectively.

2.2. Torque–speed curves for variable stiffness

An important outcome of the presented simplification is the fact that the torque–speed curves described in Appendix B can be used to represent the stationary motions of the compacting machine. As a relevant particularity of the simplified vibrocompaction model, note that the stiffness k_i is not a fixed parameter, but can take different values between k_0 and k_f, depending on the degree of compaction achieved (Fig. A.2). Then, instead of a single curve for the vibration torque, there will be a family of curves, one of them for each possible value of the mixture stiffness.

Although, in principle, the system can exhibit any stiffness between k_0 and k_f, the range of possible values for this parameter is actually narrower during the vibrocompaction. The reason lies in the fact that there is already some static compaction before the motor is switched on, due to the weight of the masses located above the spring—mainly the weight of the piston. Using k_{st} to denote the spring stiffness after the static compaction, it is clear that, during the dynamic compaction process, the stiffness can take values $k_i \in [k_{st}, k_f]$.

The vibration torque curves for the vibrocompacting machine can be obtained by using Eq. (B.6), which is rewritten here for the case of variable stiffness:

$$L_v(k_i, \Omega_0) \equiv k_i \xi_i \left(\frac{m_1 r}{m}\right)^2 \frac{\left(\frac{\Omega_0}{\omega_{ni}}\right)^5}{\left[\left(\frac{\Omega_0}{\omega_{ni}}\right)^2 - 1\right]^2 + \left[2\xi_i \frac{\Omega_0}{\omega_{ni}}\right]^2} \quad \text{for} \quad k_i \in [k_{st}, k_f], \tag{4}$$

with $\omega_{ni} = \sqrt{k_i/m}$ and $\xi_i = b/(2m\omega_{ni})$. A careful analysis of Eq. (4) reveals that the resonance peak of the curve grows approximately in proportion to $k_i^{3/2}$, while the resonance frequency ω_n is proportional to $k_i^{1/2}$. This is reflected in Fig. 3, where several vibration torque curves are plotted for growing values of the spring stiffness. Note in this figure, as will generally be the case for the rest of the article, that the dependence of L_v and L_m on Ω_0 is not explicitly written, for convenience in the notation.

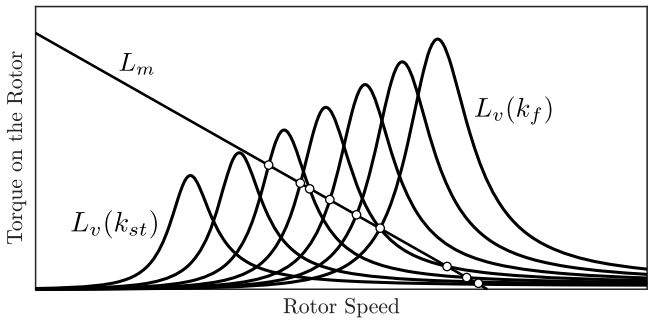

Fig. 3. Torque–speed curves for the vibrocompaction process. L_m represents the motor characteristic, while curves $L_v(k_i)$ represent the vibration torque, given in Eq. (4), for different possible values of the stiffness of the mixture (this stiffness increases as the mixture gets compacted). The possible stationary motions are marked with dots.

The collection of curves in Fig. 3 is a representative set of the whole family of curves for $k_i \in [k_{st}, k_f]$. If the torque–speed curve of the motor is depicted on the same plot, the possible stationary motions of the machine are graphically obtained as the intersections between the motor curve and each one of the vibration curves.

As shown in Fig. 3, there are many feasible stationary motions for the system. In fact, the amount of possibilities is infinite if all the curves for continuously increasing stiffness are considered. The next section will address the problem of finding, analytically, which of these infinite possible solutions is actually exhibited by the machine during a compaction process.

3. Analytical investigation of the Sommerfeld effect in a quasistatic vibrocompaction process

This section is intended to analyse a particular type of vibrocompaction process, where the control settings of the motor are very slowly varied. Then, it is first convenient to say a word about the motor control. An electric motor of any kind is controlled by means of one or more input magnitudes (current, voltage, frequency...). For example, the speed of a 3-phase induction motor is usually controlled by modifying the amplitude and frequency of the stator voltage through a variable frequency drive. For each setting of the motor control, the motor characteristic is fixed. In the presented model, where the motor curve is assumed to be given by a straight line, the motor control would allow changing parameters C and D (see Eq. (2)).

Suppose that the effect of the chosen control method consists in displacing the motor characteristic parallel to itself, i.e. changing parameter C while keeping a fixed slope D. As mentioned in Section 1.2, this is actually the case in the simplest control approach for an induction motor, known as the V/f control [63].

Now, consider a situation where the motor characteristic is very slowly displaced upwards, occupying at different time instants the positions L_{m1}, L_{m2}, L_{m3}... as represented in Fig. 4. This change in the motor control is assumed to occur quasistatically, in the sense that it does not produce any transient effects in the machine, but only a succession of stationary states. Let us focus on one particular time instant of the process, say the one at which the motor curve is given by L_{m2}. As observed in Fig. 4, several stationary solutions are possible in principle. Note that there are actually infinite potential stationary motions for L_{m2}, since the mixture stiffness, k_i, varies in a continuous manner. However, for clarity of exposition, we will consider only 3 stiffness values and, therefore, 3 possible stationary solutions for L_{m2} (marked with squares in Fig. 4). The question that will be addressed in this section is the

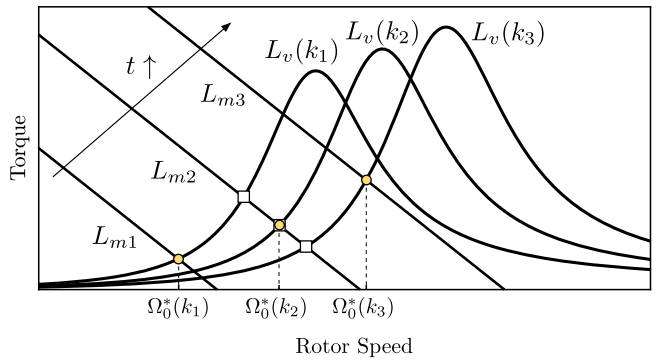

Fig. 4. Torque–speed curves along a generic quasistatic compaction process. L_{mi} ($i = 1,2,3$) represent the motor characteristic at successive time instants, while $L_v(k_i)$ ($i = 1,2,3$) are the vibration torque curves for increasing mixture stiffness. The squares mark the possible stationary motions for L_{m2}. The yellow dots represent the quasistatic stationary motion for each considered stiffness value.

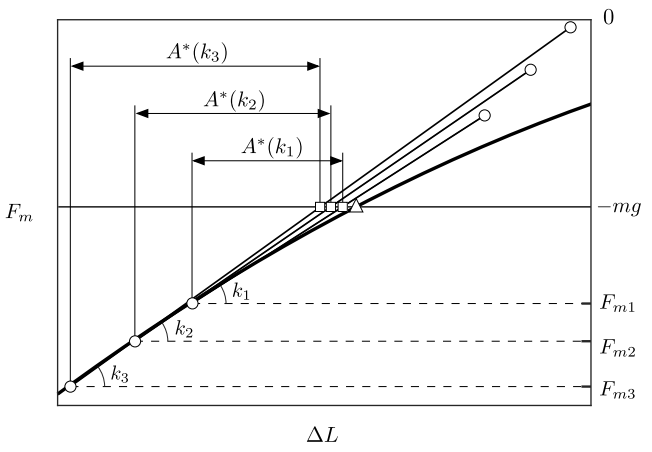

Fig. 5. Quasistatic compaction represented on the force–displacement graph of the nonlinear spring that models the mixture behaviour. k_i ($i = 1,2,3$), represents 3 increasing stiffness values of the mixture. $A^*(k_i)$ represents the quasistatic oscillation amplitude for each considered stiffness. F_{mi} represents the maximum compressive force experienced by the spring during the quasistatic oscillation for each considered stiffness. The term mg represents the weight of all the masses in the model located above the spring. The static equilibrium position for each considered stiffness is marked with square. The initial state of the system, before the motor is switched on, is marked with a triangle.

following: which of the 3 mentioned solutions is actually reached by the system during the quasistatic compaction process? In other words, how can we analytically predict which of the possible stationary motions, for each specific position of the motor characteristic, is actually exhibited by the machine during the quasistatic process?

Before entering the core of the discussion, an additional consideration is relevant. We assume that the evolution of the state of the system during the quasistatic compaction is of the same type as in the classical Sommerfeld's test, described in Section 1.2 and represented in Fig. 1: the amplitude of the oscillations grows monotonically until reaching a point where a jump phenomenon occurs, making the vibration amplitude decrease abruptly. This assumption will be confirmed by the results presented in Section 4.

This Section is divided in two subsections. In the first one, we develop the concept of *quasistatic torque curve* and present a method to calculate it. This curve provides the succession of stationary states of the machine during the quasistatic process. The second subsection investigates the maximum compaction that can be quasistatically achieved and presents the specific way in which the Sommerfeld effect occurs in the vibrocompaction system under study.

3.1. The quasistatic torque curve

In a quasistatic compaction process, the system is initially at rest, under the static load produced by the weight of all its elements. In the force–displacement graph of Fig. 5, this initial point is marked with a triangle (see Appendix A for details on this constitutive law). Then, the motor is switched on and its input power is slowly increased, producing a gradual increment in the mixture stiffness as it gets compacted. Fig. 5 represents the stationary oscillation for the 3 stiffness values considered in Fig. 4. The motion is depicted as a straight segment, with slope k_1, k_2 or k_3, delimited by the maximum and minimum displacements reached during the system vibration (circular markers in the figure). Note the important feature that, according to Fig. 5, the minimum displacement reached by the spring during the stationary vibration for stiffness k_i coincides with the tangency point between the parabola and the elastic line corresponding to stiffness k_i. This requires some detailed justification.

For each specific stiffness value, the stationary vibration necessarily takes place around the position of static equilibrium of the system, as highlighted in Fig. 5 with square markers (the static equilibrium position can always be obtained as the intersection between the elastic line of interest and the horizontal line given by $F_m = -mg$). Then, parameter $A^*(k_i)$ is defined as the displacement between the static equilibrium position and the tangent point of the elastic line with the parabola for stiffness k_i (see Fig. 5):

$$A^*(k_i) \equiv \frac{-mg - F_{mi}}{k_i} \tag{5}$$

where F_{mi} represents the value of F_m at which the parabolic curve of the spring exhibits a slope k_i.

Let us now justify that, for stiffness k_i, the stationary oscillation amplitude is given by $A^*(k_i)$. First, it is clear that this oscillation amplitude cannot be greater than $A^*(k_i)$, because that would imply following some length of the parabolic path, with the subsequent increase in the spring stiffness. On the other hand, a stationary oscillation amplitude lower than $A^*(k_i)$, for stiffness k_i, would require a decrease in oscillation amplitude over time. This is, however, not possible under the hypotheses of this study, since we assume the vibration amplitude to grow monotonically until experiencing a jump phenomenon (as was put forth previously in this section). Hence, if we focus on the portion of the process previous to the jump, a reduction in oscillation amplitude cannot take place.

We have shown that the stationary oscillation amplitude for stiffness k_i cannot be greater nor lower than $A^*(k_i)$, if the attention is restricted to the fraction of the compaction before the jump phenomenon. The obvious conclusion is that the spring stiffness grows continuously with the amplitude of the oscillation being given, for each instantaneous k_i, by $A^*(k_i)$. Since the oscillation amplitude for each k_i is known, the rotor speed $\Omega_0^*(k_i)$ can also be computed by using Eq. (B.4), which is rewritten here for convenience:

$$A^*(k_i) = \frac{\frac{m_1}{m} r \left(\frac{\Omega_0^*(k_i)}{\omega_{ni}}\right)^2}{\sqrt{\left[\left(\frac{\Omega_0^*(k_i)}{\omega_{ni}}\right)^2 - 1\right]^2 + \left[2\xi_i \frac{\Omega_0^*(k_i)}{\omega_{ni}}\right]^2}}, \tag{6}$$

where $\omega_{ni} = \sqrt{k_i/m}$ and $\xi_i = b/(2m\omega_{ni})$. Notice that there may be two possible rotor speeds for the same vibration amplitude, as observed in Fig. B.2(a). Then, care should be taken to choose the pre-resonant solution, which is the one of interest for the process under analysis (see Fig. 4).

The conclusion from all the above considerations is that, when the system reaches stiffness k_i through the quasistatic procedure being

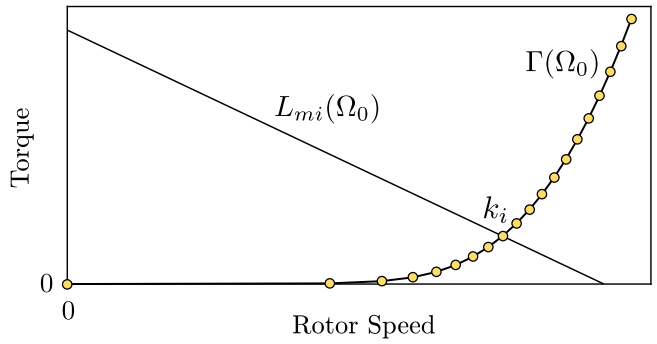

Fig. 6. Quasistatic torque curve, $\Gamma(\Omega_0)$, representing the complete sequence of motions along the quasistatic compaction. Each point of the curve is associated with a different value of the mixture stiffness (the stiffness increases upwards along the curve). $L_{mi}(\Omega_0)$ represents a motor characteristic that would allow reaching stiffness k_i, corresponding to the intersection point between $L_{mi}(\Omega_0)$ and $\Gamma(\Omega_0)$.

described, it will do so with rotor speed $\Omega_0^*(k_i)$, which can be computed using Eqs. (5) and (6). Then, going back to Fig. 4, we can represent the stationary solution corresponding to each considered stiffness value (yellow dots in the graph). Recall now that we were trying to find which of the 3 possible stationary solutions for the motor curve L_{m2}, marked with squares in Fig. 4, is actually reached by the machine during a quasistatic compaction process. By comparing these 3 square markers with the 3 yellow dots in Fig. 4, the answer becomes clear. The stationary motion of the system, when the motor curve is L_{m2}, is the one corresponding to stiffness k_2. This is the only stiffness value whose corresponding vibration torque curve $L_v(k_i)$ intersects L_{m2} at speed $\Omega_0^*(k_i)$.

Going one step further, very relevant information can be extracted by focusing on the sequence of yellow dots in Fig. 4: a new curve $\Gamma(\Omega_0)$ can be constructed by plotting the quasistatic stationary solutions for the different stiffness values, representing the complete sequence of motions followed by the machine during the quasistatic compaction. In what follows, this new curve, $\Gamma(\Omega_0)$, will be denoted as *the quasistatic torque curve* of the system.

The proposed procedure to compute the quasistatic torque curve is as follows:

- Select a set of increasing, equally spaced, stiffness values k_i ($i = 1, 2, \dots, N$) with $k_1 = k_{st}$ and $k_N = k_f$.
- Obtain, for each stiffness k_i, the corresponding quasistatic rotor speed $\Omega_0^*(k_i)$, by using relations (5) and (6).
- Obtain, for each pair of values $\{k_i, \Omega_0^*(k_i)\}$, the quasistatic torque as $\Gamma(\Omega_0^*(k_i)) = L_v(k_i, \Omega_0^*(k_i))$ by using Eq. (4).
- Represent the points given by $(\Omega_0^*(k_i), \Gamma(\Omega_0^*(k_i)))$ on a torque–speed graph and connect the points using straight lines or splines.

This gives rise to a graph such as shown in Fig. 6.

It should be stressed that the quasistatic torque curve gives very relevant information from a practical perspective. Each point of the curve corresponds to a particular stiffness and, therefore, to a particular degree of compaction. Then, the curve reveals the required driving torque to achieve the desired degree of compaction through a quasistatic process. For instance, reaching stiffness k_i in Fig. 6 would require a motor characteristic such as $L_{mi}(\Omega_0)$.

3.2. Maximum quasistatic compaction and Sommerfeld effect

It is interesting to analyse the end points of the quasistatic torque curve because, as will be seen, they provide very meaningful information about the possibilities of compaction. First, it is clear that, for stiffness k_{st}, the stationary solution is given by $\Omega_0 = 0$, $L_v = 0$, corresponding to the initial state of the machine, with the motor

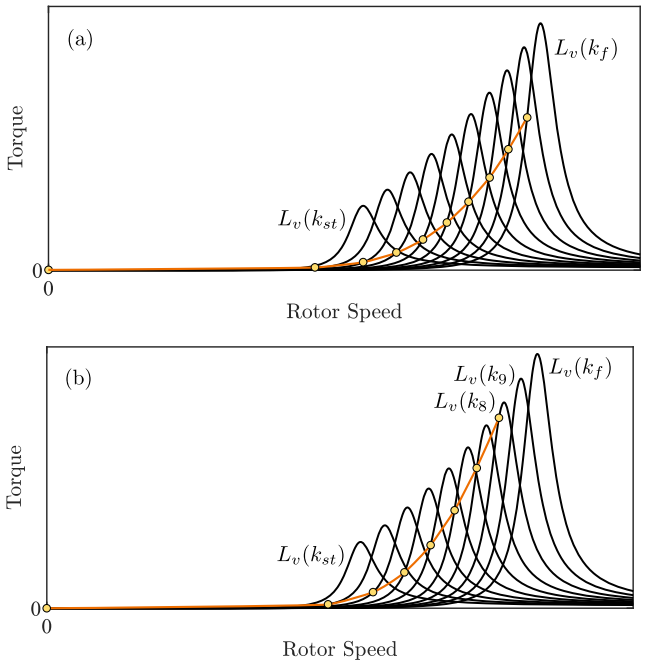

Fig. 7. Quasistatic compaction represented on a torque–speed graph. The collection of black curves represent the vibration torque curves for a set of increasing stiffness values, from k_{st} to k_f. The yellow dots represent the quasistatic stationary motion for each considered stiffness. The orange curve represents the quasistatic torque curve, $\Gamma(\Omega_0)$.
(a) Case $k_{\max} = k_f$
(b) Case $k_{\max} < k_f$.

at rest. Thus, curve $\Gamma(\Omega_0)$ starts at $(0, 0)$. In order to investigate the final point of the quasistatic torque curve, consider the torque–speed graphs in Fig. 7. Note that, in this figure, the quasistatic torque curve is represented together with the collection of vibration torque curves for a set of 10 equally spaced stiffness values between k_{st} and k_f. In principle, we should expect the quasistatic torque curve to end at the point associated with the stiffness of the totally compacted mixture, k_f (this is the situation represented in Fig. 7(a)). However, another possibility also exists. Consider the case shown in Fig. 7(b), where it can be observed that the quasistatic point associated with stiffness k_8 is already close to the maximum of the corresponding vibration torque curve. For k_9 and k_f, no quasistatic point is marked because its corresponding vibration amplitude $A^*(k_i)$ (obtained through Eq. (5)), turns out to be greater than that of the resonance peak. Then, when $\Omega_0^*(k_i)$ is tried to be computed through relation (6), no solution is found. In physical terms, it can be said that, for stiffness k_9 or k_f to be reached through a quasistatic process, the system would need to stationarily oscillate with greater amplitude than that of the resonance peak, which is not possible. Then, for the situation depicted in Fig. 7(b), the end point of the quasistatic torque curve is given by certain stiffness $k_{\max} \in (k_8, k_9)$ such that the corresponding quasistatic vibration amplitude, $A^*(k_{\max})$ coincides with that of the resonance peak.

Generalizing the above considerations, we can define parameter $k_{\max}$ as the maximum stiffness between k_{st} and k_f such that the system of Eqs. (5), (6) has a solution. This critical value $k_{\max}$ has a very meaningful interpretation: it is the maximum stiffness that can be achieved through a quasistatic compaction process. Observe that, since the motor parameters do not appear in Eqs. (5) and (6), $k_{\max}$ has the significant feature of being completely independent of the available power of the electric motors.

Clearly, two situations are possible: if $k_{\max} = k_f$, the quasistatic torque curve is qualitatively as represented in Fig. 7(a) and a complete compaction can be quasistatically achieved. Conversely, if $k_{\max} < k_f$,

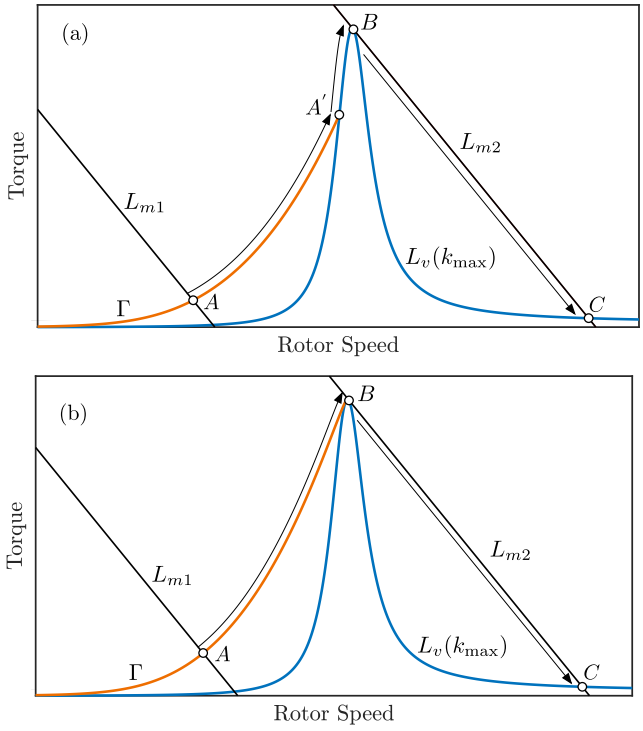

Fig. 8. Sommerfeld effect in a quasistatic vibrocompaction process. As the motor characteristic is displaced from L_{m1} to L_{m2}, the evolution of the state of the system is given by the black arrows. When tangency point B is reached, the system experiences a jump towards the post-resonant point C.
(a) Case $k_{\max} = k_f$
(b) Case $k_{\max} < k_f$.

the quasistatic torque curve is qualitatively as shown in Fig. 7(b) and the mixture cannot be totally compacted through a quasistatic procedure.

The definition of $k_{\max}$ can be directly extended to the level of compaction achieved, γ, defined in Eq. (A.6):

$$\gamma_{\max} = \frac{k_{\max} - k_0}{k_f - k_0}. \tag{7}$$

At this point, we already have all the required tools to describe how the Sommerfeld effect occurs in the vibrocompacting system under study. Consider a quasistatic compaction process in which the motor characteristic is displaced well beyond the point at which the mixture reaches stiffness $k_{\max}$. As represented in Fig. 8, the system initially follows the quasistatic torque curve as the mixture stiffness gradually increases. After stiffness $k_{\max}$ is reached, the state of the system necessarily evolves on the vibration torque curve $L_v(k_{\max})$—as has been justified in the above paragraphs, the stiffness cannot keep increasing—until reaching the point at which the motor characteristic is tangent to $L_v(k_{\max})$ (point B in Fig. 8). Past this point, no more stationary solutions are found near the resonance peak, which makes the system jump towards the only remaining stationary solution, corresponding to a post-resonant motion with small oscillation amplitudes (jump from point B to point C in Fig. 8). This is precisely the jump phenomenon observed by Sommerfeld in 1904 [31], and one of the most well-known effects of nonideal excitations, as described in Section 1.2.

It should be noted that the portion of the process between reaching stiffness $k_{\max}$ and finding the jump phenomenon, which is clearly observable for $k_{\max} = k_f$ (see path from A' to B in Fig. 8(a)), is almost nonexistent for $k_{\max} < k_f$ (see Fig. 8(b)). The reason is that, when $k_{\max} < k_f$, the quasistatic point corresponding to $k_{\max}$ coincides with the maximum of the amplitude–frequency curve, which is very close to the maximum of curve $L_v(k_{\max})$ and, consequently, also very close to the tangency point (point B in Fig. 8).

By comparing Fig. 8 to Fig. 2 in the introduction of the paper, the peculiar way in which the Sommerfeld effect takes place in the vibrocompaction system becomes apparent. For a vibrating system with fixed stiffness, such as the one studied by Sommerfeld and Kononenko [31, 34], the state of the system evolves on the vibration torque curve until encountering a jump, as represented in Fig. 2. However, in the vibrocompaction system under study, part of this evolution does not take place on a vibration torque curve, but on the quasistatic torque curve of the system, as shown in Fig. 8. This is due to the fact that, during this portion of the process, the stiffness of the vibrating system is not fixed, but gradually increases as the mixture gets compacted.

Let us summarize the main conclusions of this section. The concept of *quasistatic torque curve* has been presented, together with a procedure for its computation. This curve characterizes the evolution of the state of the vibrocompaction system along a quasistatic compaction process. It also provides the amount of motor torque required to reach a desired compaction level, together with the maximum compaction that can be quasistatically attained. This maximum value was found to be independent of the available power of the electric motors. Finally, the quasistatic torque curve reveals the specific manner in which the Sommerfeld effect takes place in the vibrocompacting machine.

After the analysis of the quasistatic compaction presented in this section, it is reasonable to wonder what the differences are when the process is not quasistatic. This would be the case, for instance, if the motor was switched on with the driving torque curve being directly in its final position, or if the control settings of the motor were abruptly modified. In these situations there can be significant transient effects influencing the evolution of the system state and, therefore, affecting the level of compaction achieved. Some of these transient effects will be discussed in the next section.

4. Results and discussion

As was commented in the Introduction, this paper builds upon a previous publication of the authors [13], where the model presented in Appendix A was described in detail, justified and investigated by means of various simulations.

The research presented in [13] was based on a numerical approach to the problem: the equations of motion (A.1) were numerically integrated for different sets of parameters values and the results were discussed and analysed. The present section intends to complement these simulations with useful analytical insight into the model. Section 4.1 summarizes the numerical results that were obtained in [13]. In Section 4.2, a clear physical interpretation for these results is provided, based on the developments of Sections 2 and 3. Analytical predictions are also verified by comparing them to the numerical results.

4.1. Summary of previous numerical results

The simulations presented in [13] were conducted by numerically solving system (A.1) for $t \in [0, t_f]$. The total time t_f includes three different stages ($t_f = t_1 + t_2 + t_3$):

- Stage 1: $t \in [0, t_1]$. Parameter C of the motor control is linearly increased from C_0 to C_f, while keeping slope D constant (see Eq. (2)). Note that this can correspond to the quasistatic process described in Section 3, as long as t_1 is long enough. The motor characteristic at the beginning and at the end of this phase are denoted as L_{m0} and L_{mf}, respectively.
- Stage 2: $t \in [t_1, t_1 + t_2]$. Parameter C is kept constant ($C = C_f$). During this phase, the vibrocompacting machine reaches a stationary motion.
- Stage 3: $t \in [t_1 + t_2, t_f]$. The system returns to rest after the motor is switched off at $t = t_1 + t_2$.

Table 1
Parameter values that remain constant through the different simulations: m_m stands for the mass of the mixture, m_p is the mass of the piston and the motor, r is the eccentricity of the unbalance, b is the damping coefficient, d_f and F_f represent, respectively, the spring deformation and spring force corresponding to a complete compaction, R_k is the ratio between the minimum and maximum values for the spring stiffness and t_2 and t_3 represent the time length of the second and third stages of the simulation, respectively.

m_m (kg)	240
m_p (kg)	1500
r (m)	0.1
b (Ns/m)	$4 \cdot 10^3$
d_f (m)	-0.1
F_f (N)	-10^5
R_k	0.1
t_2 (s)	15
t_3 (s)	15

It is useful to define a new parameter, ω_{np}, as the natural frequency exhibited by the system during stage 2. It can be calculated as

$$\omega_{np} = \sqrt{\frac{k_p}{m_p + m_m/3 + m_1}}, \tag{8}$$

where k_p denotes the stiffness exhibited by the nonlinear spring during the stationary vibration attained at stage 2.

Five different simulations are considered. Some of the system parameters are the same for the 5 cases, and their values are displayed in Table 1. The parameters that vary among the different simulations are shown in Table 2, together with the result of each simulation quantified through the final level of compaction γ_s (see definition in Eq. (A.6), subscript s stands for *simulation*).

The obtained results are graphically represented in Fig. 9 for Cases 1–4 and in Fig. 10 for Case 5, which is the only one in which separations and impacts occur between piston and mixture.

4.2. Discussion and comparison with analytical results

In this subsection, we use the developments of Sections 2 and 3 to interpret the presented numerical results. In particular, it will be shown how the quasistatic torque curve, $\Gamma(\Omega_0)$, constitutes a useful tool to understand and quantify the behaviour of the vibrocompacting machine.

Note that, among the varying parameters in Table 2, the only one that affects the vibration torque curves of the system, $L_v(k_i)$, is the unbalanced mass m_1, as can be observed in Eq. (B.6). Since m_1 is the same for Cases 1–4 and takes a different value for Case 5 (see Table 2), there will be one set of vibration torque curves for Cases 1–4 and a different set of curves for Case 5. These curves are computed through relation (B.6) for 20 equally spaced stiffness values from k_{st} to k_f and are represented in Fig. 11 together with the motor characteristics for the different simulations.

Once the vibration torque curves are obtained, the procedure described in Section 3 can be followed to compute the quasistatic stationary motion corresponding to each considered stiffness value (yellow dots in Fig. 11). By connecting these points, the quasistatic torque curve, $\Gamma(\Omega_0)$, is obtained (orange line in Fig. 11). Finally, we can use Eq. (7) to calculate parameter $\gamma_{\max}$, defined as the maximum compaction level that can be reached quasistatically:

$$\begin{aligned} \gamma_{\max}^{\text{Cases 1–4}} &= 48.2\% \\ \gamma_{\max}^{\text{Case 5}} &= 71.8\% \end{aligned} \tag{9}$$

Based on these representations and computations, the global behaviour of the system can be described as follows. If the motor characteristic passes through the end point of the quasistatic torque curve, then the mixture will reach the compaction level given in Eq. (9), as long as the motor control is sufficiently slow. This will happen as the system experiences an increasingly growing vibration amplitude followed by a jump phenomenon towards a post-resonant state of motion. On the other hand, if the motor characteristic does not reach the end point of the quasistatic torque curve, the final compaction level of the mixture will be lower than given in Eq. (9). The level of compaction achieved can be computed by introducing the maximum stiffness exhibited by the nonlinear spring into relation (A.6). This stiffness can in turn be obtained as the stiffness corresponding to the intersection point between curves $L_{mf}(\Omega_0)$ and $\Gamma(\Omega_0)$ (see square markers in Fig. 11). The application of the described procedure to the five considered simulations yield the analytical predictions presented in Table 3.

It is interesting to note that a comparison between Case 1 and Cases 2–4 provides useful insight into the effect of parameters C and D, which define the motor characteristic, on the system behaviour. As Fig. 11(a) shows, the motor characteristic passes through the end point of the quasistatic torque curve in Case 1, but not in Cases 2–4. Therefore, the analytical prediction is that the mixture attains its maximum quasistatic compaction in Case 1, but not in Cases 2–4 (see Table 3). Likewise, the system experiences a jump towards a post-resonant motion in Case 1 (see Fig. 9(a) and (b)), but not in Case 2 (see Fig. 9(c) and (d)) or Case 4 (see Fig. 9(g) and (h)). The numerical results for Case 3 do display the jump (see Fig. 9(e) and Fig. 9(f)), but in this scenario the analytical prediction does not apply because the motor control is not quasistatic (the ramp-up time, t_1, has been reduced to zero, as shown in Table 2). The effect of parameters C and D on the system dynamics will be discussed in more detail in the next paragraphs, by separately analysing each of the simulation scenarios.

For Case 1, it is clear from Fig. 11 that the motor characteristic L_{mf} passes over the end point of the quasistatic torque curve. Hence, we should expect the system to exhibit a gradually increasing vibration amplitude followed by a jump phenomenon towards a post-resonant motion with smaller amplitude. Note that this is precisely the behaviour found in the simulation results plotted in Fig. 9(a) and Fig. 9(b).

Regarding the analytical prediction for the level of compaction achieved in Case 1, a comparison between Tables 2 and 3 shows some difference with respect to the numerical result. This indicates that the process may not have been slow enough to be considered as quasistatic. To validate this hypothesis, the simulation was repeated after increasing parameter t_1 to 50 s. This produced a level of compaction $\gamma_s = 48.0\%$, which is significantly closer to the analytical value given in Table 3. This supports the idea that, the slower the displacement of the motor characteristic, the more similar the process is to the ideal quasistatic case.

Case 2 constitutes a compacting process where the motor characteristic does not pass through the end point of the quasistatic torque curve. This means that we should expect an increasing vibration amplitude during stage 1 (without any jump phenomena), followed by a stabilization during stage 2 into a stationary oscillation with the rotor speed being slightly below the system resonance frequency. This is in accurate agreement with the numerical results depicted in Fig. 9(c) and Fig. 9(d). Note also the precise accordance between the analytical and numerical evaluations of the final compaction level (compare Tables 2 and 3 for Case 2).

Case 3 has the same parameter values as Case 2 except for time t_1, which is now set to 0 (see Table 2). This means that there is no motor control: the motor characteristic is set to its final position from the beginning of the process. Thus, the simulation cannot be considered as quasistatic, which is why no analytical prediction is given in Table 3 for this case.

In any case, it is interesting to compare the numerical results of Cases 2 and 3, in order to assess the effect that a reduction of the ramp-up time can have on the machine behaviour. As clearly shown in Fig. 9, two different types of behaviour arise in these two simulations. While

Table 2
Parameter values that vary among the different simulations: m_1 is the unbalanced mass, I_0 is the rotor inertia, t_1 is the time length of the first simulation stage, D is the slope of the motor characteristic and C_0 and C_f represent the initial and final values for the motor stall torque. The final compaction level γ_s obtained in each case is also shown.

		Case 1	Case 2	Case 3	Case 4	Case 5
Variable Parameters	m_1 (kg)	20	20	20	20	40
	I_0 (kgm^2)	0.84	0.84	0.84	2.52	0.84
	t_1 (s)	10	15	0	0	15
	D (Nm/s)	−5	−1.5	−1.5	−1.5	−2.3
	C_0 (N m)	20	22	22	22	40
	C_f (N m)	140	43	43	43	80
Numerical Results	γ_s	46.5%	47.4%	44.6%	47.4%	60.3%

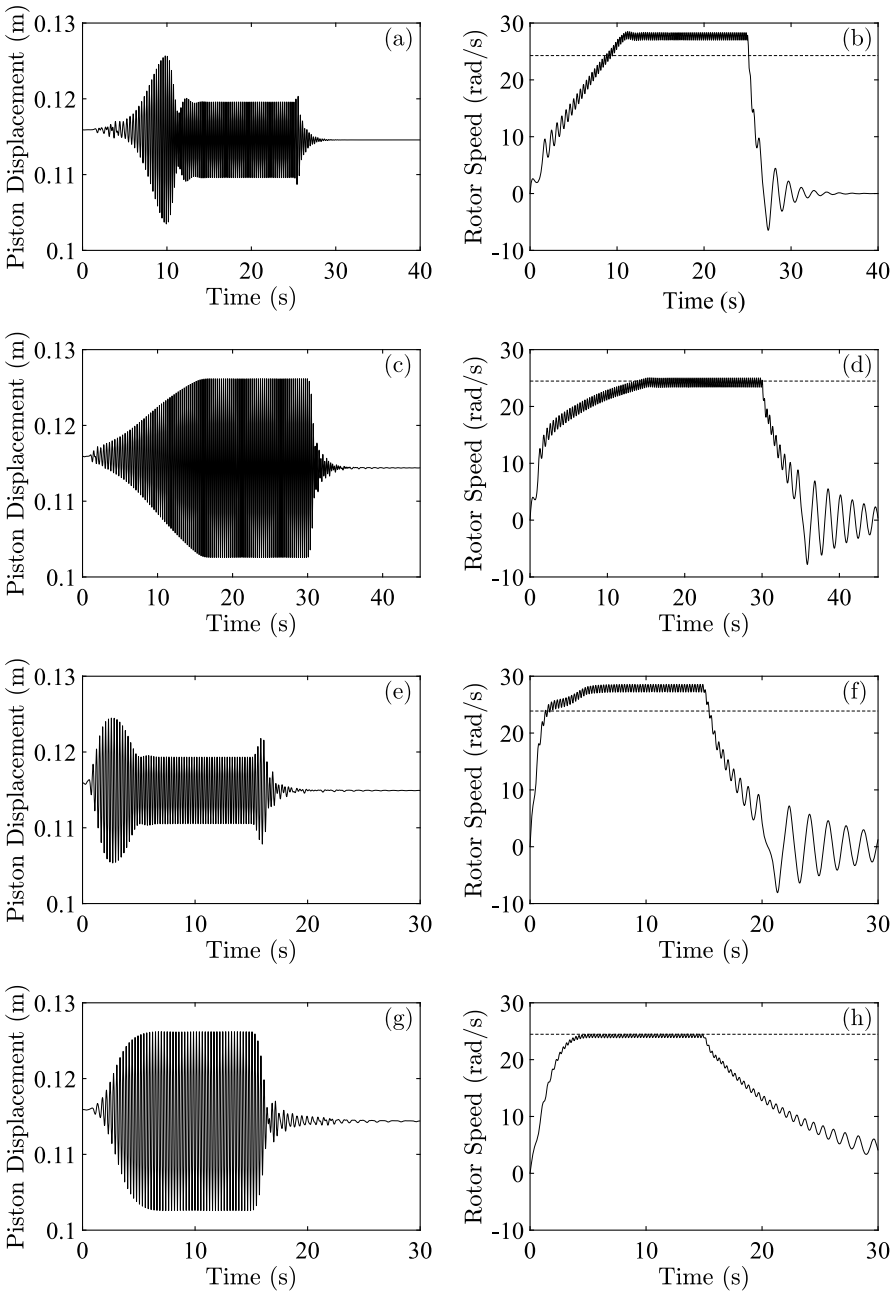

Fig. 9. Simulation results from numerical integration of system (A.1). Graphs on the left represent the displacement of the piston, while graphs on the right represent the rotor speed. From top to bottom, the results correspond to Cases 1, 2, 3 and 4. The dashed line represents the natural frequency of the system during the stationary oscillation, ω_{np}, as defined in Eq. (8).

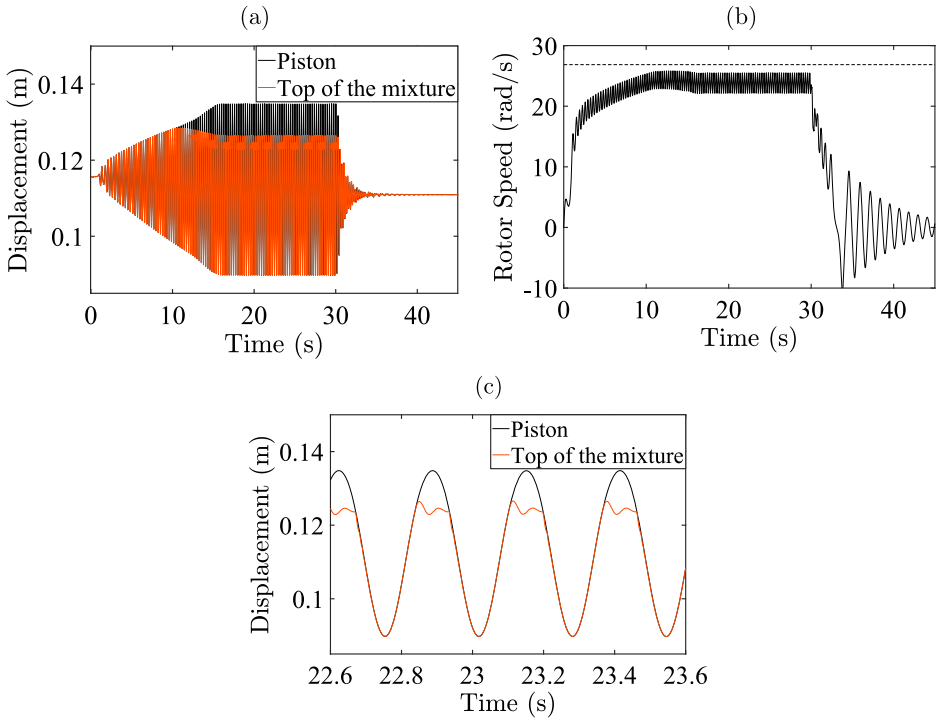

Fig. 10. Simulation results corresponding to Case 5, obtained by numerical integration of system (A.1). (a) Vertical displacement of the piston and the top surface of the mixture (separations and impacts are observed between 10 s and 30 s approx.). (b) Rotor speed. The dashed line represents the natural frequency of the system during the stationary oscillation, ω_{np}, as defined in Eq. (8). (c) Close-up view of the piston and mixture displacements, showing clearly the separations and impacts.

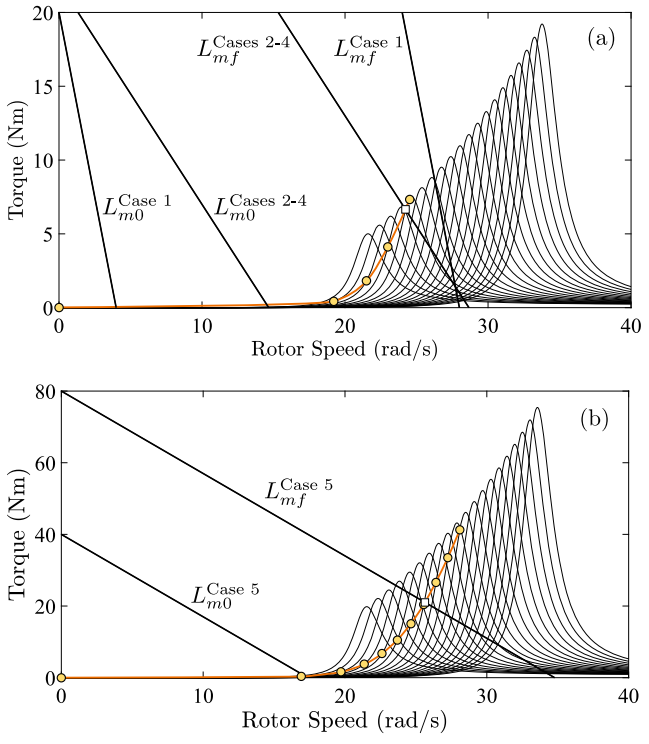

Fig. 11. Torque–speed curves for (a) Cases 1–4 and (b) Case 5. The black straight lines represent the motor characteristic at the beginning (L_{m0}) and at the end (L_{mf}) of stage 1. The collection of black curves with a peak represent a group of vibration torque curves, $L_v(k_i)$, for different equally spaced stiffness values (the leftmost and rightmost curves corresponds to stiffness k_{st} and k_f, respectively). The yellow dots mark the quasistatic stationary motion for each of the considered stiffness values. The orange curve represents the quasistatic torque curve, $\Gamma(\Omega_0)$. The intersection between $\Gamma(\Omega_0)$ and the motor characteristic L_{mf}, if it exists, is marked with a square.

Table 3
Analytically predicted compaction level, γ_a, for the 5 cases under study. No result is given for Case 3 because it cannot be considered as quasistatic.

	Case 1	Case 2	Case 3	Case 4	Case 5
γ_a	48.2%	47.3%	–	47.3%	58.9%

in Case 2 the system stabilizes into a stationary motion slightly below resonance, in Case 3 the system passes through resonance and stabilizes into a stationary motion with lower vibration amplitude. Note also in Table 2 that Case 3 yields a lower compaction level.

The explanation for the fact that the system passes through resonance in Case 3 might be in the difference between the characteristic time of the rotor speed and the vibration amplitude. If the rotor speed is a much faster variable than the vibration amplitude, then it can be expected that the rotor speed will reach the resonance region while the vibration amplitude is still relatively small. In this situation, the system might be attracted towards a post-resonant stationary motion with relatively small vibration amplitude, as displayed in Fig. 9(e) and Fig. 9(f). Case 4 is intended to validate the above explanation.

In Case 4, all parameters are as in Case 3, except for an increased rotor inertia (see Table 2). Interestingly, the results presented in Fig. 9(g) and Fig. 9(h) show that the system does not pass through resonance in Case 4. In fact, the machine is found to stabilize into the same stationary oscillation as in Case 2 (see Fig. 9) and reaches the same compaction level as in Case 2 (see Table 2).

What is peculiar about Case 4 is that the system exhibits the kind of quasistatic evolution discussed in Section 3, even though there is no motor control. In other words, a large rotor inertia can play the same role as a gentle displacement of the motor characteristic. This in turn confirms the explanation that was put forth for the passage through resonance in Case 3: a larger rotor inertia clearly slows down the increase of the rotor speed from zero up to the resonance frequency, which can provide sufficient time for the rise of the vibration amplitude, allowing the system dynamics to be attracted towards a near-resonant state.

Case 5 is relevant because the unbalanced mass m_1 is doubled with respect to all other cases, as shown in Table 2. This has a clear consequence in terms of the vibration torque curves of the system: when the unbalanced mass is doubled, the vibration torque curves are scaled up by a factor of 4 (compare Fig. 11(b) with Fig. 11(a)). This relation can be plainly seen in Eq. (B.6), which shows that the vibration torque, L_v, is proportional to m_1^2.

The analytical prediction for Case 5 is as follows: Fig. 11 shows that the motor characteristic does not reach the end point of the quasistatic torque curve. Hence, we should expect a monotonic increase in rotor speed and vibration amplitude until the system stabilizes into a stationary motion slightly below resonance. This matches the numerical behaviour represented in Fig. 10, with the particularity that separations and impacts between piston and mixture are found in the simulation results. It is clear that a higher unbalanced mass increases the amplitude of the exciting force on the piston, which in turn facilitates the appearance of separations and impacts at the contact surfaces.

By comparing the analytical and numerical compaction levels for Case 5 (see Tables 2 and 3), the accuracy of the analytical prediction is found to be lower than in previous cases. This can be easily explained by the fact that the analytical procedure developed in Section 3 is based on the simplified vibrocompaction model, which assumes no separations between mixture and piston nor between mixture and mould. Then, it is reasonable to expect the accuracy of analytical results to decrease when separations and impacts do take place during the process. In spite of this, note that the analytical results are still fairly close to the numerical ones in the present case. Hence, the torque–speed curves may be useful even for scenarios where impacts are produced, keeping in mind that the analytical predictions will not be as accurate as in a case of continuous contact.

It is also interesting to consider how the overall dynamics of the system changes around resonance due to the presence of separations and impacts. One observable effect is the reduction in rotor speed, as shown in Fig. 10(b) between $t \approx 12\,\mathrm{s}$ and $t \approx 17\,\mathrm{s}$. The reason is that the piston oscillates with a larger amplitude than it would if separations were not allowed. This in turn produces a larger resisting torque on the motor due to vibration and, therefore, a lower average rotor speed. In addition, it is worth noting that the numerical level of compaction turns out to be greater than it would be in the absence of impacts, which can be observed by comparing Tables 2 and 3 for Case 5. This is consistent with the physical intuition that impacts are favourable to the compaction process, since they produce high peaks of compressive force on the mixture.

Finally, a brief discussion on the role of nonlinearity in the presented developments is pertinent. One of the sources of nonlinearity in the full model given by Eq. (A.1) is the possibility of having separations and impacts between the different contacting surfaces. While this nonlinearity is taken into account in the presented numerical results (see Fig. 10), it is not considered in our analytical predictions, since these are based upon an assumption of continuous contact. On the other hand, the nonlinearity associated with the hardening constitutive law for the mixture is included in both the numerical and analytical approaches (see Fig. 11, where the vibration torque curve changes as the mixture gets compacted). Another source of nonlinearity in our analysis is the nonideal interaction between the electric motor and the vibrating system, which is responsible for the presence of the Sommerfeld effect. This nonlinearity is included both in the numerical and analytical results. The analytical treatment of the nonideal excitation is based on Blekhman's direct separation of motions approach, which is summarized in Appendix B. Additional sources of nonlinearity that could be included in further developments are the friction between quartz particles in the mixture or the motion of air bubbles through the resin. Explicitly modelling these effects would amount to proposing a more complex constitutive law than the one used here.

Regarding future work on the problem addressed in this article, we plan to conduct some experimental tests to validate the presented analytical and numerical results.

5. Summary and conclusions

A simplified 4-DOF model previously published by the authors is used in this article to analytically investigate the influence of the Sommerfeld effect on vibrocompaction processes driven by unbalanced electric motors. The model includes a nonideal interaction between motor and vibrating system and a nonlinear constitutive law for the mixture being compacted, which accounts for irreversible deformation and hardening due to compaction.

The main novel contribution of the paper is the development of the concept of *quasistatic torque curve* and its calculation. This curve characterizes the evolution of the system state during a quasistatic compaction process (i.e. one controlled by a sufficiently slow increase of the motors input power) and predicts the appearance of the Sommerfeld effect in the vibrocompacting machine.

Another relevant feature of the quasistatic torque curve is that it provides the amount of motor torque required to reach a desired level of compaction, together with the maximum compaction that can be quasistatically reached. This maximum compaction was found to be independent of the available power of the electric motors.

The obtained analytical results were used to give a clear physical interpretation to the numerical results previously published by the authors using the same model. Good agreement was found between numerical and analytical results. In this regard, it should be mentioned that the accuracy of the analytical results decreases with the presence of separations and impacts between mixture and piston and between mixture and mould, since the quasistatic torque curve is built upon the assumption of continuous contact. However, even in a compaction process with severe impacts, the analytical predictions proved to be reasonably close to the corresponding numerical results.

CRediT authorship contribution statement

Javier González-Carbajal: Study conception & design, Material preparation, Analytical development, Numerical simulations. **Daniel García-Vallejo:** Study conception & design, Material preparation, Analytical development, Numerical simulations. **Jaime Domínguez:** Study conception & design, Material preparation, Analytical development, Numerical simulations.

Declaration of competing interest

The authors declare that they have no known competing financial interests or personal relationships that could have appeared to influence the work reported in this paper.

Data availability

Data will be made available on request

Acknowledgement

All authors discussed the results and contributed to the final manuscript.

Funding

This work was supported by the Spanish Ministry of Education, Culture and Sport (grant number FPU12/00537).

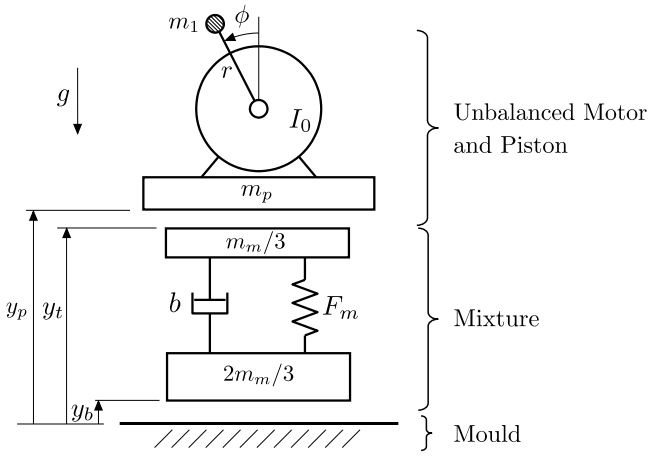

Fig. A.1. 4-DOF model of the vibrocompaction system. The 4 degrees of freedom are ϕ (angular position of the rotor), y_p (vertical position of the piston), y_t (vertical position of the top surface of the mixture) and y_b (vertical position of the bottom surface of the mixture). The spring labelled as F_m has a nonlinear behaviour that models compaction itself.

Appendix A. Brief description of the vibrocompaction model

The vibrocompaction model that was presented and justified in [13] is summarized here. As can be observed in Fig. A.1, the quartz-resin mixture is represented in the model by a couple of masses attached to each other through a linear damper and a nonlinear spring, which models compaction itself by allowing for permanent deformation under compression. Then, the distance between the masses represents the thickness of the mixture slab. The mould is modelled as a rigid base, while the piston with the unbalanced motors is represented by a mass with a single unbalanced motor. The mixture is in contact—with separations and impacts allowed—with the mould at the bottom and the piston at the top. The vacuum system and the external air pressure on the piston are not included in the model.

As represented in Fig. A.1, the model has 4 DOFs: y_b, y_t, y_p and ϕ, which correspond, respectively, to position of the bottom surface of the mixture, position of the top surface of the mixture, position of the piston and rotation of the motor.

The parameters in Fig. A.1 are as follows: m_m stands for the mass of the mixture, m_1 is the unbalanced mass, m_p is the mass of the piston and the motor, r is the eccentricity of the unbalance, I_0 is the rotor inertia, b is the damping coefficient, F_m is the force produced by the nonlinear spring and g is the gravity constant. The fact that the mixture mass is distributed as shown in Fig. A.1—two thirds at the bottom, one third at the top—is justified in [13].

The equations of motion of the system can be shown to be

$$\begin{aligned}(m_p+m_1)\ddot{y}_p &= m_1 r(\dot{\phi}^2\cos\phi+\ddot{\phi}\sin\phi)+F_{ct}(y_t,\dot{y}_t,y_p,\dot{y}_p)-(m_p+m_1)g\\ \frac{m_m}{3}\ddot{y}_t+F_m+b(\dot{y}_t-\dot{y}_b) &= -F_{ct}(y_t,\dot{y}_t,y_p,\dot{y}_p)-\frac{m_m}{3}g\\ \frac{2m_m}{3}\ddot{y}_b-F_m-b(\dot{y}_t-\dot{y}_b) &= F_{cb}(y_b,\dot{y}_b)-\frac{2m_m}{3}g\\ I\ddot{\phi} &= L_m(\dot{\phi})+m_1 r\sin\phi(\ddot{y}_p+g)\end{aligned} \tag{A.1}$$

where $I = I_0 + m_1 r^2$, $L_m(\dot{\phi})$ is the driving torque and F_{cb}, F_{ct} represent the normal contact force between mixture and mould and between mixture and piston, respectively. A Hunt and Crossley model is chosen for these contacts (see [13] for details):

$$\left\{\begin{array}{ll} F_{ct}=k_c(y_t-y_p)+b_c(y_t-y_p)(\dot{y}_t-\dot{y}_p) & \text{if } y_t>y_p\\ F_{ct}=0 & \text{if } y_t\le y_p\end{array}\right\} \tag{A.2}$$

$$\left\{\begin{array}{ll} F_{cb}=-k_c y_b+b_c y_b\dot{y}_b & \text{if } y_b<0\\ F_{cb}=0 & \text{if } y_b\ge 0\end{array}\right\} \tag{A.3}$$

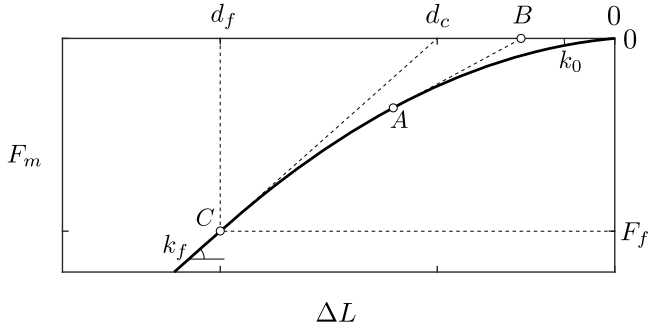

Fig. A.2. Constitutive law for the nonlinear spring (spring force F_m vs axial deformation ΔL). The material follows a parabolic hardening line as it gets compacted and a tangent straight line during relaxation. Point $C(d_f, F_f)$ defines the complete compaction, which occurs once the mixture has reached its maximum stiffness k_f.

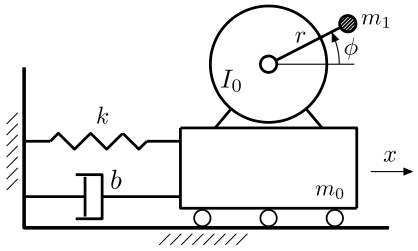

Fig. B.1. Schematic representation of the considered mechanical system: an unbalanced motor with known torque–speed curve connected to a fixed frame through a linear spring and a linear damper. The system has 2 degrees of freedom: linear displacement x and rotation ϕ.

The driving torque of the motor is assumed to be a linear function of the rotor speed:

$$L_m(\dot{\phi}) = C + D\dot{\phi}, \tag{A.4}$$

with $D < 0$. Expression (A.4) represents the torque–speed curve of the motor, or motor characteristic.

Regarding the behaviour of the nonlinear spring, a phenomenological model is used in agreement with the two main observed features of compaction:

- When a compressive force is applied on the material, it deforms in a nonlinear hardening manner.
- If the compressive load is released, some of the deformation remains (irreversible deformation due to compaction) while the rest is recovered (elastic deformation).

The proposed constitutive model is represented in Fig. A.2, which shows the relation between the spring force, F_m, and the spring deformation, ΔL, defined as

$$\Delta L \equiv y_t - y_b - L_0 \tag{A.5}$$

where L_0 is the undeformed length of the spring.

The behaviour is as follows. Starting from the undeformed position O, a compressive force makes the spring follow a parabolic hardening path, with an initial tangent stiffness k_0. Suppose that, at an intermediate state of compaction A, the compression force reduces until reaching an unloaded state. The spring follows the straight line AB, which is tangent to the parabolic curve at point A. Note that, at this stage, the spring stiffness has already increased with respect to the initial value k_0. Note also that, at point B, some plastic deformation remains, corresponding to the level of compaction achieved, while the elastic part of the deformation has been recovered.

If a compressive load is applied again, the material deforms along the elastic path BA, followed by the hardening parabolic line. The

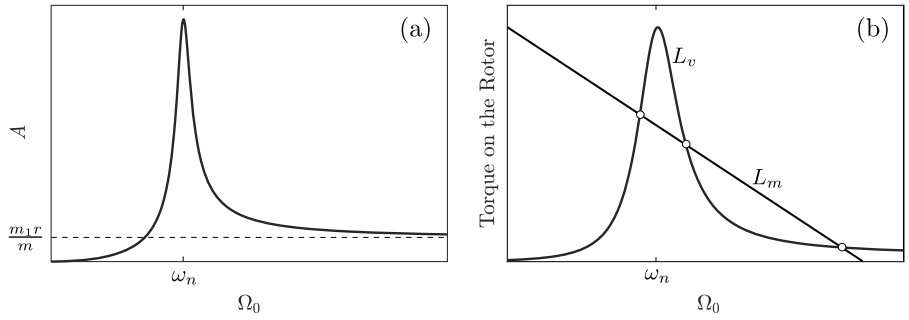

Fig. B.2. Response curves of a linear system under the nonideal excitation of an unbalanced motor. (a) Amplitude of the stationary vibration versus average rotor speed (Eq. (B.4)). (b) Torque–speed curves for a typical case with three intersection points. L_m and L_v represent the motor torque (Eq. (A.4)) and the torque due to vibration (Eq. (B.6)), respectively. The intersections, marked with circles, give the possible values of the average stationary rotor speed, Ω_0.

complete compaction is defined by point $C(d_f, F_f)$, where the tangent nonlinear stiffness is k_f. Whenever point C is reached, the mixture becomes totally compacted, and any subsequent loading would only produce elastic deformations with stiffness k_f. Note that the spring behaviour is completely defined by specifying F_f, d_f and $R_k \equiv k_0/k_f$.

Finally, it is useful to characterize the quality of a particular vibrocompaction process by the level of compaction achieved, defined as

$$\gamma = \frac{k_p - k_0}{k_f - k_0} \tag{A.6}$$

where k_p is the spring stiffness once the dynamic compaction process is finished. Thus, $\gamma = 0$ corresponds to a totally uncompacted mixture, while $\gamma = 1$ represents a case of complete compaction.

The presented constitutive model is in qualitative agreement with the experimental results reported in [64,65]. On the other hand, it is clear that many other types of curves could be proposed to model the hardening line, instead of a parabola. Some models in the literature use exponential [66] or inverse-logarithmic laws [67], as described by Kiesgen et al. [68]. Some work should be done in the future comparing experimental results on the compression of quartz-resin mixtures with different types of curves, in order to see which one provides better fitting.

Appendix B. Stationary response of a linear system to the nonideal excitation of an unbalanced motor

This appendix summarizes previous results on the response of linear systems to nonideal excitations that are useful for the analysis of vibrocompaction. The presented results are based on Blekhman's approach of *direct separation of motions* [52]. For a detailed derivation of these solutions, see [52] or Chapter 7 in [62].

Consider the system depicted in Fig. B.1, where variable x stands for the linear motion, ϕ is the angle of the rotor, m_1 is the unbalanced mass with eccentricity r, m_0 is the rest of the vibrating mass, I_0 is the rotor inertia (without including the unbalance), b is the viscous damping coefficient and k is the spring stiffness. The equations of motion for this 2-DOF system can be shown to be [37]

$$\begin{aligned} m\ddot{x} + b\dot{x} + kx &= m_1 r(\dot{\phi}^2 \cos\phi + \ddot{\phi}\sin\phi) \\ I\ddot{\phi} &= L_m(\dot{\phi}) + m_1 r\ddot{x}\sin\phi \end{aligned} \tag{B.1}$$

with $m = m_0 + m_1$ and $I = I_0 + m_1 r^2$. Function $L_m(\dot{\phi})$ is the driving torque produced by the motor, given by Eq. (A.4).

It should be stressed that, although the vibrating structure is linear (elastic and viscous forces are proportional to displacement and velocity), the application of a nonideal excitation makes the combined *vibrating structure + motor* system nonlinear, as clearly seen in Eq. (B.1).

Under the condition of *small unbalance* ($m_1 \ll m$, $m_1 r^2 \ll I$), the stationary motions of the system can be written as [52]

$$\begin{aligned} \dot{\phi}(t) &= \Omega_0 + \Omega_1(t) \\ x(t) &\approx A\cos(\Omega_0 t + \psi), \end{aligned} \tag{B.2}$$

where $\Omega_1(t)$ is a periodic function of time with zero average satisfying

$$\left.\begin{array}{l} \Omega_1(t) \ll \Omega_0 \\ \dot{\Omega}_1(t) \ll \Omega_0^2 \end{array}\right\} \forall t. \tag{B.3}$$

The oscillation amplitude is given by

$$A = \frac{\frac{m_1}{m} r \left(\frac{\Omega_0}{\omega_n}\right)^2}{\sqrt{\left[\left(\frac{\Omega_0}{\omega_n}\right)^2 - 1\right]^2 + \left[2\xi\frac{\Omega_0}{\omega_n}\right]^2}} \tag{B.4}$$

where $\omega_n = \sqrt{k/m}$ and $\xi = b/(2m\omega_n)$. Eq. (B.4), which corresponds to a very well-known result from linear vibration theory, is graphically represented in Fig. B.2(a).

The average rotor speed Ω_0 can be found as the intersection between two curves:

$$L_m(\Omega_0) = L_v(\Omega_0), \tag{B.5}$$

where function $L_m(\Omega_0)$ is given at Eq. (A.4) and function $L_v(\Omega_0)$ has the expression [52]

$$L_v(\Omega_0) \equiv k\xi\left(\frac{m_1 r}{m}\right)^2 \frac{\left(\frac{\Omega_0}{\omega_n}\right)^5}{\left[\left(\frac{\Omega_0}{\omega_n}\right)^2 - 1\right]^2 + \left[2\xi\frac{\Omega_0}{\omega_n}\right]^2}. \tag{B.6}$$

The physical meaning of Eq. (B.5) is very relevant: the average stationary rotor speed is such that the driving torque delivered by the motor (L_m) is equal to the resisting torque on the rotor due to vibration (L_v). This is graphically represented in Fig. B.2(b) for a typical situation with three possible stationary motions.

References

[1] Arnold M, Herle I. Comparison of vibrocompaction methods by numerical simulations. Int J Numer Anal Methods Geomech 2009;33(16):1823–38.
[2] Belnoue JP-H, Valverde MA, Onoufriou M, Sun XR, Ivanov DS, Hallett SR. On the physical relevance of power law-based equations to describe the compaction behaviour of resin infused fibrous materials. Int J Mech Sci 2021;199:106425.
[3] Khoei A, Biabanaki S, Parvaneh S. Dynamic modeling of powder compaction processes via a simple contact algorithm. Int J Mech Sci 2012;64(1):196–210.
[4] Martin C, Bouvard D. Isostatic compaction of bimodal powder mixtures and composites. Int J Mech Sci 2004;46(6):907–27.
[5] Lee S, Kim K. Densification behavior of aluminum alloy powder under cold compaction. Int J Mech Sci 2002;44(7):1295–308.
[6] Basarab V. Study of the dynamical parameters of vibration machine for compaction of construction mixes. Int Appl Mech 2020;56(6):750–61.
[7] Page J, Djelal C, Vanhove Y. Optimisation of vibrocompaction process for wood-based concrete blocks. Int J Adv Manuf Technol 2020;109(3):1189–204.
[8] Lu Q, Wang Y-Z. Nonlinear solitary waves in particle metamaterials with local resonators. J Acoust Soc Am 2022;151(3):1449–63.
[9] Lu Q, Wang Y-Z. Nonreciprocal head-on collision between two nonlinear solitary waves in granular metamaterials with an interface. Acta Mech Solida Sin 2022;1–13.

[10] Wei L-S, Wang Y-Z, Wang Y-S. Nonreciprocal transmission of nonlinear elastic wave metamaterials by incremental harmonic balance method. Int J Mech Sci 2020;173:105433.

[11] Ribeiro CEG, Rodriguez RJS, de Carvalho EA. Microstructure and mechanical properties of artificial marble. Constr Build Mater 2017;149:149–55.

[12] Silva FS, Ribeiro CEG, Rodriguez RJS. Physical and mechanical characterization of artificial stone with marble calcite waste and epoxy resin. Mater Res 2017;21.

[13] González-Carbajal J, García-Vallejo D, Domínguez J. Nonlinear modelling and simulation of vibrocompaction processes. Int J Non-Linear Mech 2018;102:101–11.

[14] Balthazar JM. Nonlinear vibrations excited by limited power sources. Springer; 2022.

[15] da Cunha Demartini TJ, Rodríguez RJS, Silva FS. Physical and mechanical evaluation of artificial marble produced with dolomitic marble residue processed by diamond-plated bladed gang-saws. J Mater Res Technol 2018;7(3):308–13.

[16] Ribeiro C, Rodríguez R, Vieira C, de Carvalho E, Candido V, Monteiro S. Production of synthetic ornamental marble as a marble waste added polyester composite. Mater Sci Forum 2014;341–5. http://dx.doi.org/10.4028/www.scientific.net/MSF.775-776.341.

[17] Lee M-Y, Ko C-H, Chang F-C, Lo S-L, Lin J-D, Shan M-Y, et al. Artificial stone slab production using waste glass, stone fragments and vacuum vibratory compaction. Cem Concr Compos 2008;30(7):583–7. http://dx.doi.org/10.1016/j.cemconcomp.2008.03.004.

[18] Peng L, Qin S. Mechanical behaviour and microstructure of an artificial stone slab prepared using a SiO2 waste crucible and quartz sand. Constr Build Mater 2018;171:273–80.

[19] Gomes Ribeiroa CE, Sanchez Rodriguez RJ. Influence of compaction pressure and particle content on thermal and mechanical behavior of artificial marbles with marble waste and unsaturated polyester. Mater Res 2015;18:283–90. http://dx.doi.org/10.1590/1516-1439.372314.

[20] Shishegaran A, Saeedi M, Mirvalad S, Korayem AH. The mechanical strength of the artificial stones, containing the travertine wastes and sand. J Mater Res Technol 2021;11:1688–709.

[21] Tong L, Qi B, Xu C. Fluidity characteristic of granular materials within low frequency dynamics. Int J Mech Sci 2021;202:106508.

[22] Tong L, Qi B, Ding H, Xu C. Statistical model predicts softening and fluidization induced by vibration in granular materials. Int J Mech Sci 2020;171:105373.

[23] Nejadsadeghi N, Misra A. Axially moving materials with granular microstructure. Int J Mech Sci 2019;161:105042.

[24] Grégoire C, Correia AG, De Bel R, Dethy B. Mechanical behavior of natural and recycled granular materials for roads. J Test Eval 2011;39(5):792–802.

[25] Tran-Duc T, Ho T, Thamwattana N. A smoothed particle hydrodynamics study on effect of coarse aggregate on self-compacting concrete flows. Int J Mech Sci 2021;190:106046.

[26] Alonso EE, Gens A, Josa A. A constitutive model for partially saturated soils. Géotechnique 1990;40(3):405–30. http://dx.doi.org/10.1680/geot.1990.40.3.405.

[27] Pietruszczak S, Pande GN. Constitutive relations for partially saturated soils containing gas inclusions. J Geotech Eng 1996;122(1):50–9. http://dx.doi.org/10.1061/(ASCE)0733-9410(1996)122:1(50).

[28] Stickel JJ, Powell RL. Fluid mechanics and rheology of dense suspensions. Annu Rev Fluid Mech 2005;37(1):129–49. http://dx.doi.org/10.1146/annurev.fluid.36.050802.122132.

[29] Zhang J, Shen W, Zhu Q, Shao J-F. A homogenized macroscopic criterion for shakedown analysis of ductile porous media with kinematical hardening matrix. Eur J Mech A Solids 2020;82:104015.

[30] Acary V, Bourrier F. Coulomb friction with rolling resistance as a cone complementarity problem. Eur J Mech A Solids 2021;85:104046.

[31] Sommerfeld A. Naturwissenchftliche ergebnisse der neuren technischen mechanik. Verein Deutscher Ingenieur Z. 1904;18:631–6.

[32] Cveticanin L, Zukovic M. Motion of a motor-structure non-ideal system. Eur J Mech A Solids 2015;53:229–40.

[33] Nayfeh AH, Mook DT. Nonlinear oscillations. John Wiley & Sons; 2008.

[34] Kononenko VO. Vibrating systems with a limited power supply. London: Iliffe; 1969.

[35] Dimentberg M, McGovern L, Norton R, Chapdelaine J, Harrison R. Dynamics of an unbalanced shaft interacting with a limited power supply. Nonlinear Dynam 1997;13(2):171–87.

[36] Bolla M, Balthazar JM, Felix J, Mook D. On an approximate analytical solution to a nonlinear vibrating problem, excited by a nonideal motor. Nonlinear Dynam 2007;50(4):841–7.

[37] El-Badawy AA. Behavioral investigation of a nonlinear nonideal vibrating system. J Vib Control 2007;13(2):203–17.

[38] González-Carbajal J, Domínguez J. Non-linear vibrating systems excited by a nonideal energy source with a large slope characteristic. Mech Syst Signal Process 2017;96:366–84.

[39] González-Carbajal J, Domínguez J. Limit cycles in nonlinear vibrating systems excited by a nonideal energy source with a large slope characteristic. Nonlinear Dynam 2017;87(2):1377–91.

[40] Sghaier E, Bourdon A, Remond D, Dion J-L, Peyret N. Coupled bending torsional vibrations of non-ideal energy source rotors under non-stationary operating conditions. Int J Mech Sci 2019;163:105155.

[41] Varanis MV, Tusset AM, Balthazar JM, Litak G, Oliveira C, Rocha RT, et al. Dynamics and control of periodic and non-periodic behavior of duffing vibrating system with fractional damping and excited by a non-ideal motor. J Franklin Inst B 2020;357(4):2067–82.

[42] Avanço RH, Tusset AM, Balthazar JM, Nabarrete A, Navarro HA. On nonlinear dynamics behavior of an electro-mechanical pendulum excited by a nonideal motor and a chaos control taking into account parametric errors. J Braz Soc Mech Sci Eng 2018;40(1):1–17.

[43] Felix JLP, Balthazar JM, Rocha RT, Tusset AM, Janzen FC. On vibration mitigation and energy harvesting of a non-ideal system with autoparametric vibration absorber system. Meccanica 2018;53(13):3177–88.

[44] Piccirillo V. Improving the dynamic integrity of a non-ideal oscillator via linear vibration absorber. Eur Phys J Spec Top 2021;230(18):3493–9.

[45] Drozdetskaya O, Fidlin A. On the passing through resonance of a centrifugal exciter with two coaxial unbalances. Eur J Mech A Solids 2018;72:516–20.

[46] Bharti S, Sinha A, Samantaray A, Bhattacharyya R. The Sommerfeld effect of second kind: Passage through parametric instability in a rotor with non-circular shaft and anisotropic flexible supports. Nonlinear Dynam 2020;100:3171–97.

[47] Jha AK, Dasgupta SS. Suppression of Sommerfeld effect in a non-ideal discrete rotor system with fractional order external damping. Eur J Mech A Solids 2020;79:103873.

[48] Kong X, Jiang J, Zhou C, Xu Q, Chen C. Sommerfeld effect and synchronization analysis in a simply supported beam system excited by two non-ideal induction motors. Nonlinear Dynam 2020;100(3):2047–70.

[49] Varanis M, Silva AL, Balthazar JM, Oliveira C, Tusset A, Bavastri CA. A short note on synchrosqueezed transforms for resonant capture, Sommerfeld effect and nonlinear jump characterization in mechanical systems. J Vib Eng Technol 2021;1–6.

[50] Bharti SK, Samantaray AK. Resonant capture and Sommerfeld effect due to torsional vibrations in a double cardan joint driveline. Commun Nonlinear Sci Numer Simul 2021;97:105728.

[51] González-Carbajal J, García-Vallejo D, Domínguez J. Stability of a nonideally excited duffing oscillator. Nonlinear Dynam 2022;1–21.

[52] Blekhman II. Vibrational mechanics: Nonlinear dynamic effects, general approach, applications. World Scientific; 2000.

[53] Kong X, Li W, Jiang J, Dong Z, Wang Z. Dynamic characteristics of a simply supported elastic beam with three induction motors. J Sound Vib 2022;520:116603.

[54] Sinha A, Bharti SK, Samantaray AK, Bhattacharyya R. Sommerfeld effect in a single-DOF system with base excitation from motor driven mechanism. Mech Mach Theory 2020;148:103808.

[55] Varanis M, Balthazar J, Silva A, Mereles A, Pederiva R. Remarks on the Sommerfeld effect characterization in the wavelet domain. J Vib Control 2019;25(1):98–108.

[56] Varanis M, Mereles A, Silva AL, Barghouthi MR, Balthazar JM, Lopes EM, et al. Numerical and experimental investigation of the dynamic behavior of a cantilever beam driven by two non-ideal sources. J Braz Soc Mech Sci Eng 2020;42(10):1–18.

[57] Martino J, Harri K. Virtual shaker modeling and simulation, parameters estimation of a high damped electrodynamic shaker. Int J Mech Sci 2019;151:375–84.

[58] Kossoski A, Tusset AM, Janzen FC, Rocha RT, Balthazar JM, Brasil RM, et al. Jump attenuation in a non-ideal system using shape memory element. In: MATEC web of conferences, vol. 148, EDP Sciences; 2018, p. 03003.

[59] Balthazar JM, Mook DT, Weber HI, Fenili A, Belato D, Felix J. An overview on non-ideal vibrations. Meccanica 2003;38:613–21.

[60] Balthazar JM, Tusset AM, Brasil RM, Felix JL, Rocha RT, Janzen FC, et al. An overview on the appearance of the Sommerfeld effect and saturation phenomenon in non-ideal vibrating systems (NIS) in macro and MEMS scales. Nonlinear Dynam 2018;93(1):19–40.

[61] Sanders JA, Verhulst F, Murdock J. Averaging methods in nonlinear dynamical systems, Vol. 59. 2nd ed.. Springer; 2007.

[62] González-Carbajal J. Nonlinear vibrations produced by unbalanced motors [Ph.D. thesis], Universidad de Sevilla; 2017.

[63] Holtz J. Sensorless control of induction motor drives. Proc IEEE 2002;90(8):1359–94.

[64] Favrie N, Gavrilyuk S. Dynamic compaction of granular materials. Proc R Soc A: Math, Phys Eng Sci 2013;469(2160):20130214.

[65] Jogi V. Predictions for multi-scale shock heating of a granular energetic material [MS thesis], USA: Louisiana State University; 2003.

[66] Richard P, Nicodemi M, Delannay R, Ribiere P, Bideau D. Slow relaxation and compaction of granular systems. Nature Mater 2005;4(2):121–8.

[67] Knight JB, Fandrich CG, Lau CN, Jaeger HM, Nagel SR. Density relaxation in a vibrated granular material. Phys Rev E 1995;51(5):3957.

[68] Kiesgen de Richter S, Hanotin C, Marchal P, Leclerc S, Demeurie F, Louvet N. Vibration-induced compaction of granular suspensions. Eur Phys J E 2015;38(7):1–9.